Spatially Non-uniform Time-Step Adaptation in Unsteady Flow Problems

Karthik Mani * and Dimitri J. Mavriplis †

Department of Mechanical Engineering, University of Wyoming, Laramie, Wyoming 82071-3295

This paper presents a space-time finite-volume formulation for the Euler equations, which allows for the use of spatially non-uniform time-steps. The formulation also inherently accounts for the effect of dynamically deforming computational meshes. The space and time dimensions are treated in a unified manner so as to permit the variation of control volume sizes in both dimensions. The primary goal is to maintain solution accuracy while reducing the number of unknowns in the overall solution process and potentially lower computational expense. While the formulation presented here is capable of simultaneously handling non conformal meshes in both space and time, the scope of the paper is limited to conformal spatial meshes with non conformal temporal meshes. At any slice in time, the number of spatial elements remains the same, but across any slice in space, the number of time-steps is allowed to vary. In traditional terms, this translates to non-uniform temporal advancement of spatial elements in an unsteady problem. Two unsteady problems, one where an isentropic vortex is convected through a rectangular domain and one of a pitching NACA64A010 airfoil in transonic conditions are presented to demonstrate the algorithm. A local temporal error indicator is used to identify space-time elements which require higher resolution in the time dimension, thus marking them for temporal refinement. The results indicate that significant reduction in the overall degrees-of-freedom required to solve an unsteady problem can be achieved using the proposed algorithm. Modest improvements in computational expense for specific problems are also observed.

I. Introduction

The fundamental goal of numerical simulations is to obtain accurate solutions to nonlinear governing equations at acceptable computational expense. In the early days of the field, unsteady problems were deemed unreasonably expensive and the focus remained on accurate solutions to steady-state problems. Several algorithmic advances in terms of numerically solving nonlinear equations have been made over the years to reduce the cost associated with obtaining accurate solutions.[1,2] Such advances coupled with improved hardware capabilities have since enabled solutions to unsteady problems, firstly using explicit methods and then progressing to faster and more efficient implicit time-integration schemes. While simple unsteady problems remain tractable, problems exhibiting strong unsteadiness currently require simulation times running into days or even weeks. Several methods have been been investigated to address this issue. Higher-order implicit time-integration schemes[3–7] operate directly in the time domain and maintain solution accuracy while using fewer time-steps. For problems exhibiting strong periodic behavior, frequency domain methods[8,9] transform the unsteady problem into time spectral space and restrict the number of modes required for the solution. Solution techniques such as multigrid[10–12] have also been developed to reduce the cost associated with solving the non-linear system of equations at each each time-step. Although frequency-domain based techniques are quite powerful, their performance is inefficient when applied to problems with no dominant periodicity. This necessitates the development of improved algorithms operating in the time domain so as to be applicable to all unsteady problems in a general sense.

In the context of implicit time-integration schemes, which impose no restrictions on the time-step size, additional savings can be realized by varying the time-step size at each implicit time-step provided an estimate of the local temporal error at each time-step is available. This approach is directly analogous to the universally common practice of utilizing non-uniform spatial meshes when solving problems. It is unnecessary to use high spatial resolution in regions of very low gradients such as the far field in aerodynamic simulations. Using lower resolution in such regions immediately frees up essential resources to focus on high gradient regions such as shock waves, boundary layers contact discontinuities, and wakes that exist closer to the aerodynamic body of interest. The same argument applies

*Postdoctoral Research Associate; email: kmani@uwyo.edu.

†Professor; email: mavripl@uwyo.edu.

to the time domain and computational savings can be achieved by focusing temporal resolution on regions of the time domain where such resolution is necessary. While the locations of high gradient spatial features are to a certain extent known a priori, the locations of similar interesting features in the time domain are generally not known ahead of time and an error indicator becomes necessary.

Several methods currently exist for time-step size control based on temporal discretization error. The purpose of such methods is to adaptively change the time-step size in various regions of the time domain resulting in overall reduction in computational expense with minimal loss in solution accuracy. Local error-based methods[4,13,14] use temporal discretizations of different orders of accuracy for the time derivative term in the governing equations in order estimate the local temporal discretization error. Higher temporal resolution (i.e. smaller and more time-steps) is used in regions of the time domain where the local temporal discretization error is high and lower resolution is used in regions of low local error. Goal-based or global error-based methods[15,16] determine the distribution of the temporal discretization error that is relevant to functional quantities of interest and similarly adapt the time-step size to improve functional accuracy.

While non-uniform spacing in the time domain is essential to reducing overall simulation cost, a fundamental point that is overlooked here is that resolution in the spatial and temporal domains can be treated independently of each other. Just as spatial flow gradients are small in the far field, it should be noted that temporal gradients also remain small in these regions. Much like spatial flow gradients near the aerodynamic object of interest, it is quite likely that high temporal flow gradients also exist only close to the object. The interpretation is that spatial elements in the far field do not have to be advanced in time at the same rate as spatial elements close to the object of interest. This realization changes the traditional view on how unsteady problems are solved and opens a new avenue to explore for the reduction computational cost. Since existing error indicators (both local- and goal-based) construct the temporal discretization error at each time-step from a spatial distribution of the same at each time-step, the means already exists to identify individual spatial elements which require refinement in the time dimension.

The main hurdle is the development of efficient discretizations for the governing equations that permit non-uniform advancement in time. This paper presents a method to overcome this problem by treating the governing equations in integral form over space-time elements which have a constant cell averaged state over the entire element in space and time. While there have been a few attempts to solve the governing equations in space-time integral form,[17–19] advancing spatial elements non-uniformly in time has mostly been limited to explicit time-integration schemes.

It should be noted that in the work presented in this paper no attempt is made to adapt the spatial domain. Hence there is direct correspondence between spatial elements at different times and there are no spatial discontinuities going from one point in time to another within the same space-time element. However, there exists discontinuities in time going from one point in space to another.

II. Analysis Problem Formulation

A. Governing equations of the flow Problem in ALE form

We begin with the traditional conservative form of the Euler equations. In vectorial form the conservative form of the Euler equations may be written as:

$$\frac{\partial \mathbf{U}(\mathbf{x},t)}{\partial t} + \nabla \cdot \mathbf{F}(\mathbf{U}) = 0 \tag{1}$$

where the state vector $\mathbf{U}$ of conserved variables and the cartesian inviscid flux vector $\mathbf{F} = (\mathbf{F}^x, \mathbf{F}^y)$ are:

$$\mathbf{U} = \begin{pmatrix} \rho \\ \rho u \\ \rho v \\ E_t \end{pmatrix}, \quad \mathbf{F}^x = \begin{pmatrix} \rho u \\ \rho u^2 + p \\ \rho uv \\ u(E_t + p) \end{pmatrix}, \quad \mathbf{F}^y = \begin{pmatrix} \rho v \\ \rho uv \\ \rho v^2 + p \\ v(E_t + p) \end{pmatrix}, \tag{2}$$

Here ρ is the fluid density, (u,v) are the cartesian fluid velocity components, p is the pressure and E_t is the total energy. For an ideal gas, the equation of state relates the pressure to total energy by:

$$p = (\gamma - 1)\left[E_t - \frac{1}{2}\rho(u^2 + v^2)\right] \tag{3}$$

where $\gamma = 1.4$ is the ratio of specific heats. Applying the divergence theorem and integrating over a moving control volume $A(t)$ that is bounded by the control surface $B(t)$ yields:

$$\int_{A(t)} \frac{\partial \mathbf{U}}{\partial t} dA + \int_{B(t)} \mathbf{F}(\mathbf{U}) \cdot \mathbf{n} dB = 0 \tag{4}$$

Using the differential identity:

$$\frac{\partial}{\partial t} \int_{A(t)} \mathbf{U} dA = \int_{A(t)} \frac{\partial \mathbf{U}}{\partial t} dA + \int_{B(t)} (\dot{\mathbf{x}} \cdot \mathbf{n}) dB \tag{5}$$

equation (4) is rewritten as:

$$\frac{\partial}{\partial t} \int_{A(t)} \mathbf{U} dA + \int_{B(t)} [\mathbf{F}(\mathbf{U}) - \dot{\mathbf{x}}\mathbf{U}] \cdot \mathbf{n} dB = 0 \tag{6}$$

or when considering cell-averaged constant values within each spatial element for the state $\mathbf{U}$, as:

$$\frac{dA\mathbf{U}}{dt} + \int_{B(t)} [\mathbf{F}(\mathbf{U}) - \dot{\mathbf{x}}\mathbf{U}] \cdot \mathbf{n} dB = 0 \tag{7}$$

This is the Arbitrary-Lagrangian-Eulerian (ALE) finite-volume form of the Euler equations. The equations are required in ALE form since the problem involves deforming meshes where mesh elements change in shape and size in time. Here A refers to the area or volume of the spatial element, $\dot{\mathbf{x}}$ is the vector of spatial mesh face or edge velocities, $\mathbf{n}$ is the unit normal of the face or edge, and B refers to the area or length of the bounding surface or edge.

Since the goal is to adapt the time-step size locally for each spatial element in the mesh, the ALE finite-volume form shown in equation (7) is further integrated in time to obtain the finite-volume formulation in space-time as:

$$\int_T \left\{ \frac{dA\mathbf{U}}{dt} + \int_{B(t)} [\mathbf{F}(\mathbf{U}) - \dot{\mathbf{x}}\mathbf{U}] \cdot \mathbf{n} dB \right\} dt = 0 \tag{8}$$

where separating the time integral yields:

$$\int_T \frac{dA\mathbf{U}}{dt} dt + \int_T \int_{B(t)} [\mathbf{F}(\mathbf{U}) - \dot{\mathbf{x}}\mathbf{U}] \cdot \mathbf{n} dB dt = 0 \tag{9}$$

B. The space-time element

Figure (1) illustrates a space-time element constructed using an arbitrary spatial element ABC at two different time indices n and $n-1$. This can also be interpreted as a space-time element bounded by two temporal faces which are defined by the spatial elements ABC at the two time indices. The spatial components of the normal vector for the temporal faces are zero by definition of the problem. The space-time element is also bounded on the sides by space-time faces. These faces are inclined due to spatial mesh deformation in time and usually have nonzero spatial and temporal normal vector components. Temporal faces are bounded by spatial edges and space-time faces are bounded by both temporal and spatial edges. Temporal edges connect the tails or heads of spatial edges at different times as shown in the figure. Figure (2) illustrates an example of a space-time face. There may be multiple temporal edges between two spatial edges in time because of neighboring space-time elements which take multiple time-steps in relation to the space-time element under consideration. Every edge (temporal or spatial) connects to a space-time node. It should also be noted that the top and bottom defining spatial edges of a space-time face are always oriented in the same direction. Temporal edges are always oriented such that they point in the direction of advancing time.

C. Temporal discretization

The solution state $\mathbf{U}$ is assumed to be constant within each space-time element and hence at any interface between space-time elements in the time dimension, the solution is double valued. Based on these assumptions, the time derivative term may be discretely represented as:

$$\int_T \frac{dA\mathbf{U}}{dt} dt = \frac{dA\mathbf{U}}{dt} \Delta t \tag{10}$$

where Δt refers to the height of the space-time element in the time dimension. The time derivative term is discretized using a first-order accurate BDF1 (Backward Difference Formula 1) scheme as:

$$\frac{dA\mathbf{U}}{dt}\Delta t = A^n\mathbf{U}^n - A^{n-1}\mathbf{U}^{n-1} \tag{11}$$

where $\mathbf{U}^n$ refers to the solution state within the space-time element extending from t^{n-1} and t^n, $\mathbf{U}^{n-1}$ refers to the solution state in the lower space-time element, and A^{n-1}, A^n refer to the temporal face areas. This discretization essentially amounts to a fully upwinded flux balance in the time dimension for the space-time element under consideration, accurate up to first-order, where the unit time normal for the upper face is 1 and the unit time normal for the lower face is -1. All spatial components of the normal vector for the upper and lower temporal faces are zero by definition of the problem.

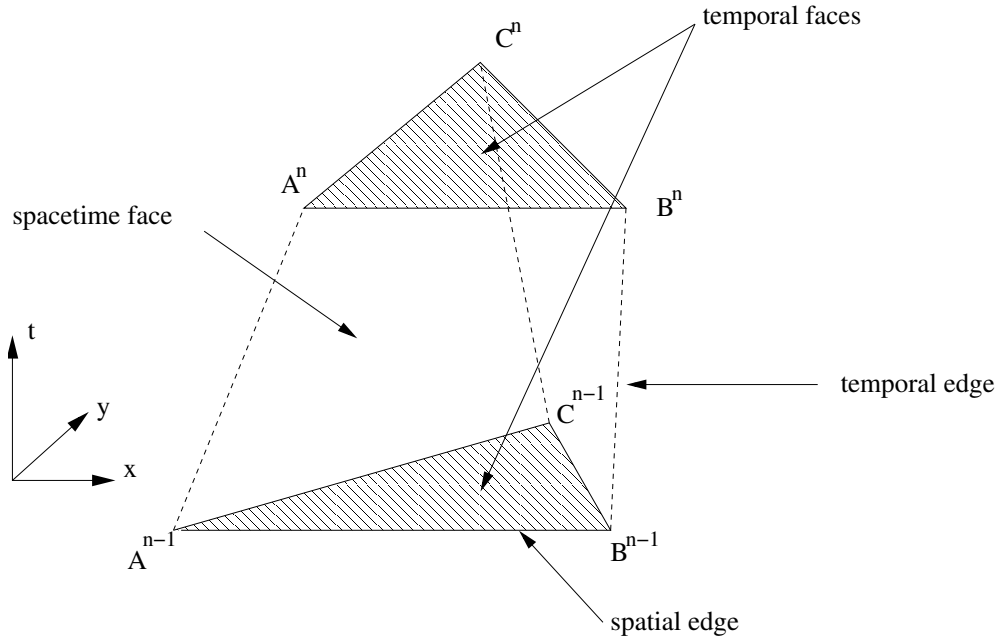

Figure 1. Example of a space-time element constructed from a spatial element at two time locations.

D. Spatial discretization

The flow solver uses a cell-centered finite-volume formulation where the inviscid flux integral S over the inclined space-time faces (i.e. with non-zero spatial components for the normal vector) bounding a space-time element is discretized as:

$$S = \int_T \int_{dB(t)} [\mathbf{F}(\mathbf{U}) - \dot{\mathbf{x}}\mathbf{U}] \cdot \mathbf{n} dB dt = \sum_{i=1}^{n_{edge}} \mathbf{F}_{e_i}^{\perp}(V_{e_i}, \mathbf{U}, \mathbf{n}_{ei}) B_{e_i} \Delta t_{e_i} \tag{12}$$

where B_e represents the L_2 norm of the spatial components of the dimensional normal vector of the face, V_e is the normal face velocity, $\mathbf{n}_e$ is the unit spatial normal vector of the face and is obtained by normalizing the dimensional spatial normal components of the face by B_e, $F_e^{\perp}$ is the normal convective flux across the face, and Δt_e is the height of the face in the time dimension. The normal convective flux across the face is computed using the second-order accurate matrix dissipation scheme[20] as the sum of a central difference and an artificial dissipation term as shown below,

$$\mathbf{F}_e^{\perp} = \frac{1}{2}\left\{\mathbf{F}_L^{\perp}(\mathbf{U}_L, V_e, \mathbf{n}_e) + \mathbf{F}_R^{\perp}(\mathbf{U}_R, V_e, \mathbf{n}_e) + \kappa^{(4)}[T]|[\lambda]|[T]^{-1}\left\{(\nabla^2\mathbf{U})_L - (\nabla^2\mathbf{U})_R\right\}\right\} \tag{13}$$

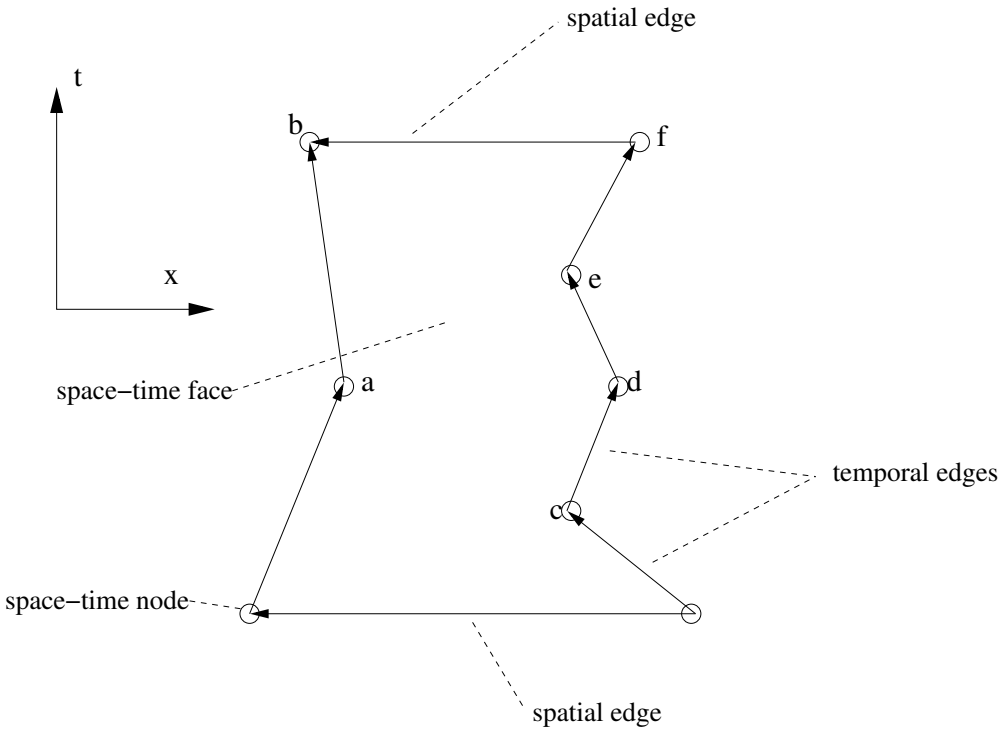

Figure 2. Example of a space-time face bounding a space-time element.

where $\mathbf{U}_L$, $\mathbf{U}_R$ are the left and right state vectors and $(\nabla^2\mathbf{U})_L$, $(\nabla^2\mathbf{U})_R$ are the left and right undivided Laplacians computed for any space-time element i as

$$(\nabla^2\mathbf{U})_i = \sum_{k=1}^{\text{spatial neighbors}} (\mathbf{U}_k - \mathbf{U}_i) \tag{14}$$

The matrix $[\lambda]$ is diagonal and consists of the eigenvalues (adjusted by normal edge velocity V_e) of the flux Jacobian matrix $\frac{\partial \mathbf{F}^\perp}{\partial \mathbf{U}}$, and the matrix $[T]$ consists of the corresponding eigenvectors. The scalar parameter $\kappa^{(4)}$ is empirically determined and controls the amount of artificial dissipation added to the centrally differenced flux. For transonic problems this is usually taken as 0.1. The advantage of using the difference of the undivided Laplacians in the construction of the convective flux is that it offers second-order spatial accuracy without the need for state reconstruction techniques. The normal native flux vector is computed as

$$\mathbf{F}^\perp = \begin{pmatrix} \rho(V^\perp - V_e) \\ \rho(V^\perp - V_e)u + \hat{n}_x p \\ \rho(V^\perp - V_e)v + \hat{n}_y p \\ E_t(V^\perp - V_e) + pV^\perp \end{pmatrix} \tag{15}$$

where the fluid velocity normal to the edge $V^\perp$ is defined as $u\hat{n}_x + v\hat{n}_y$, where $\hat{n}_x$ and $\hat{n}_y$ are the spatial components of the unit face normal vector.

E. Mesh deformation strategy

Deformation of the mesh is achieved through the linear tension spring analogy[21,22] which approximates the complete space-time mesh as a network of inter-connected springs. Every spatial and temporal edge defines a spring connected to a space-time node. The spring coefficient is assumed to be inversely proportional to the edge length. Three independent force balance equations for x, y and t are formulated for each node based on displacements of neighboring nodes. This results in a nearest neighbor stencil for the final linear system to be solved. The linear system that relates the interior

node displacements in the mesh to known displacements on the boundaries is given as

$$[\mathbf{K}]\delta\mathbf{x}_{int} = \delta\mathbf{x}_{bound} \tag{16}$$

where $[\mathbf{K}]$ is the stiffness matrix assembled using the spring coefficients of each of the edges in the computational mesh. Since the equations are decoupled between dimensions, prescribing zero displacements in the time dimension at the boundaries assures that temporal faces have zero spatial normal vector components. The linear mesh motion system is solved using Gauss-Seidel iterations and a comparison of the typical convergence of the mesh motion equations for spatial meshes and space-time meshes is shown in Figure (3).

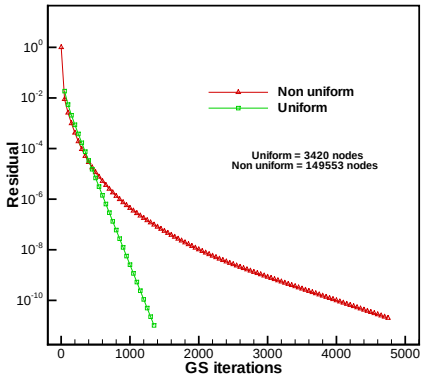

Figure 3. Typical convergence of the mesh motion linear system at a single time-step for spatially uniform time-stepping and a single slab for the case of spatially non-uniform time-stepping.

F. The discrete geometric conservation law (GCL) and space-time face normals

The discrete geometric conservation law (GCL) requires that a uniform flow field be preserved exactly when equation (9) is integrated. In other words the deformation of the computational mesh should not introduce conservation errors in the solution of the flow problem. This translates into $\mathbf{U} = constant$ being an exact solution of equation (9). The space-time face velocities and normal vectors have to be chosen such that this condition is satisfied.

The normal space-time face velocity including the spatiotemporal area of the face can be computed as follows. Collapsing the two spatial edges defining the top and bottom of a space-time face to the same time level, the face can be viewed as an area swept in x, y by a spatial edge deforming from its orientation at time index $n-1$ to its new orientation at time index n. The path followed by the head and tail nodes of the spatial edge between the two orientations is given by the spatial coordinates of the head nodes belonging to the intermediate temporal edges. The area swept by the spatial edge is computed using the Green-Gauss contour integral and used as the face velocity which includes the space-time face area.

Only the dimensional spatial components of the space-time face normal vector are required and these are computed using the time-averaged coordinates of the head and tail nodes belonging to the sweeping spatial edge between the two orientations. Choosing the space-time face normal velocities and face normal vectors in this manner assures that for a constant flow field, the governing equations discretely integrate in space-time to zero.

III. General Implementation Details

A. Space-time implicit solution procedure

Consider the normal case of uniformly advancing spatial elements in time. For the first-order BDF1 time-integration scheme, the flow equations are solved implicitly at each time-step by introducing an implicit residual $\mathbf{R}$ as:

$$\mathbf{R}^n(\mathbf{U}^n, \mathbf{U}^{n-1}, \mathbf{x}^n, \mathbf{x}^{n-1}) = 0 \tag{17}$$

which is linearized with respect to the unknown state $\mathbf{U}^n$ and solved using Newton's method as:

$$\left[\frac{\partial \mathbf{R}(\mathbf{U}^k,\mathbf{x})}{\partial \mathbf{U}^k}\right]\delta\mathbf{U}^k = -\mathbf{R}(\mathbf{U}^k,\mathbf{x}) \tag{18}$$
$$\mathbf{U}^{k+1} = \mathbf{U}^k + \delta\mathbf{U}^k$$
$$\delta\mathbf{U}^k \to 0, \mathbf{U}^{k+1} = \mathbf{U}^n$$

In the case of a uniform time-step size for all spatial elements, the state vector $\mathbf{U}$ for each spatial element is unknown at time-index n but is known at the previous time index $n-1$. The solution procedure involves constructing the nonlinear residual $\mathbf{R}$ for each spatial element at the time index n and solving for the state $\mathbf{U}^n$ using Newton's method, where the intermediate linear systems arising in the non-linear solution are solved approximately using Gauss-Seidel iterations. Figures (4(a)) and (4(b)) illustrate the uniform advancement in time with and without the presence of spatial mesh deformation in time for a spatially one-dimensional problem.

In the case of spatially nonuniform time stepping, neighboring spatial elements are advanced in time at different rates. The solution procedure for such a problem involves first the division of the time domain into slabs of some predetermined temporal spacing and then subdividing certain space-time elements appropriately in the time dimension when additional temporal resolution is required. The temporal slab thickness is chosen such that essential nonlinearities in the time dimension are captured. The advancement in time is now carried out from slab to slab, where the solution state $\mathbf{U}$ for all space-time elements in a particular slab are solved for simultaneously in an implicit manner before moving onto the next slab in time. The residual operator for a slab can be written as:

$$\mathbf{R}^n(\mathbf{U}^n,\mathbf{U}^b,\mathbf{x}^n,\mathbf{x}^b) = 0 \tag{19}$$

where the index n now refers to a temporal slab and all of the space-time elements contained within it. The index b refers to boundary values for the slab in both space and in time. The solution process involves applying Newton's method on the nonlinear residual operator $\mathbf{R}$ defined over the entire temporal slab. It is important to note that the state vectors of each space-time element in the slab under consideration are unknown and have to be obtained simultaneously irrespective of their location in time within the slab. Figures (5(a)) and (5(b)) illustrate the time advancement procedure for spatially nonuniform time stepping with and without the presence of mesh deformation. A comparison of the typical non-linear convergence of the flow equations at a single time-step for the case of uniform time-stepping and a single slab for the case of non-uniform time-stepping is shown in Figure (6).

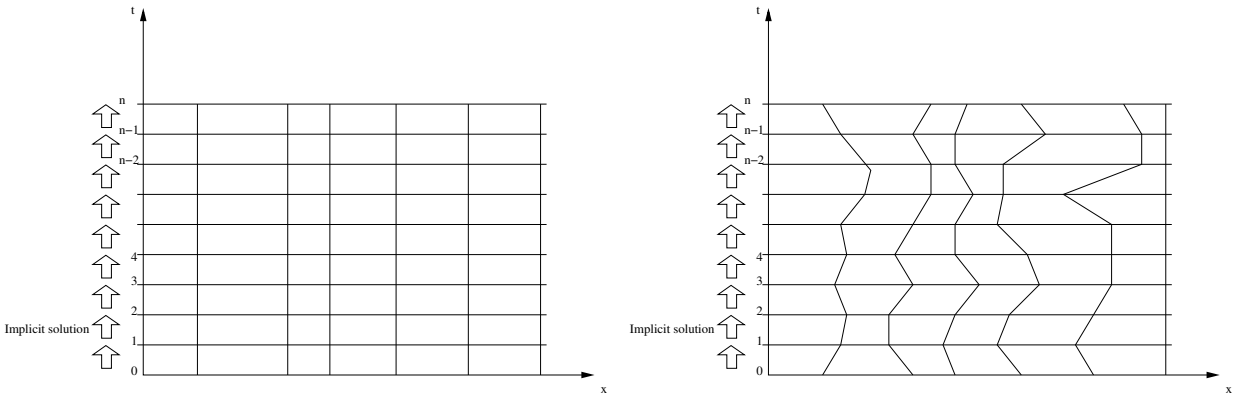

(a) Spatially uniform time stepping without mesh deformation

(b) Spatially uniform time stepping with spatial mesh deformation

Figure 4. Illustration of spatially uniform time stepping for a spatially one-dimensional problem.

B. Error indicator for adaptation

The local error indicator proposed in Ref[4] is used as the temporal discretization error indicator for adaptation purposes. The method involves obtaining a solution using the first-order BDF1 discretization of the time derivative term in the governing equations, and then reevaluating the time derivative on the basis of the obtained solution using the BDF2 time discretization. The local temporal error is then estimated as the L_2 norm of the difference between BDF1 and

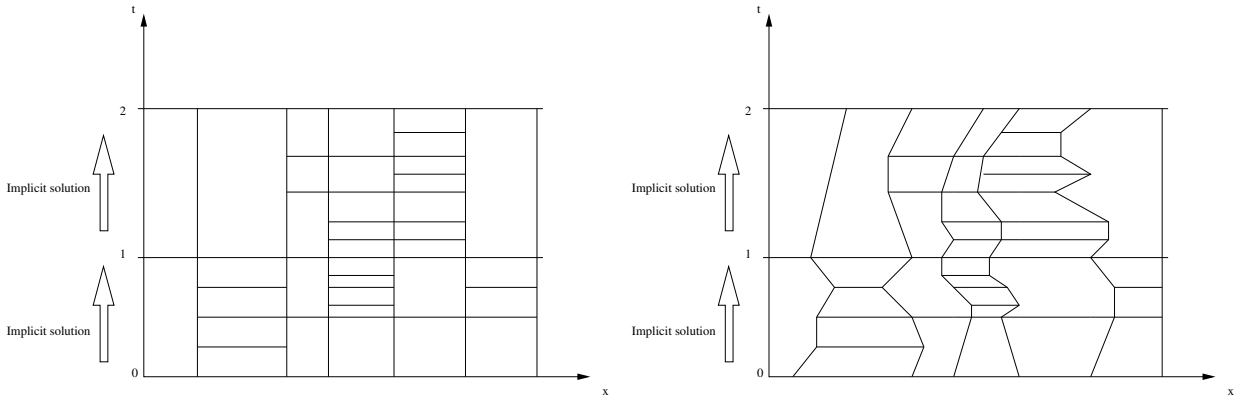

(a) Spatially nonuniform time stepping without mesh deformation (b) Spatially nonuniform time stepping with spatial mesh deformation

Figure 5. Illustration of spatially nonuniform time stepping for a spatially one-dimensional problem.

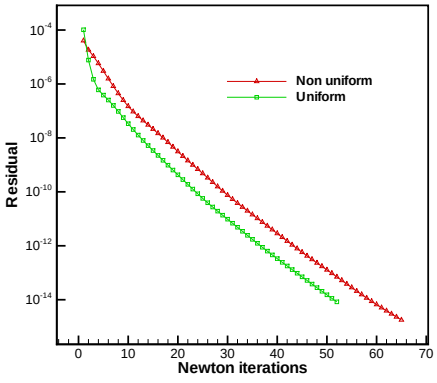

Figure 6. Typical nonlinear convergence of the flow equations at a single time-step for spatially uniform time-stepping and a single slab for the case of spatially non-uniform time-stepping. The non-uniform time-stepping solution was performed within a slab consisting of 211232 space-time elements, while the uniform time-stepping solution consisted of 6601 spatial elements. 20 Gauss-Seidel iterations were employed for the linear systems in both cases.

BDF2-based time derivative terms as shown below.

$$e_{local} = \left\| \left[\frac{d\mathbf{U}}{dt} \right]_{BDF2} - \left[\frac{d\mathbf{U}}{dt} \right]_{BDF1} \right\|_2 \tag{20}$$

Strictly speaking, this formulation is only valid for the case of static meshes. For the case of dynamic meshes, the residual operator constructed using a discretization of higher temporal order of accuracy should be used as an estimate of the local error. However, the space-time discretization developed in this work is limited to first-order temporal accuracy and a valid GCL compliant second-order accurate discretization is yet to be developed. For this reason, we choose to utilize the error indicator shown above, as is, and assume that small geometric variations in the mesh have an acceptably low impact on the estimated error.

C. Code details

The space-time adaptive solver consists of three separate codes, namely a mesh preprocessor, a mesh adaptation code and the flow solver. The mesh preprocessor takes in a standard unstructured spatial mesh and constructs a space-time mesh based on the chosen temporal parameters for the flow problem. The required temporal parameters are the number of temporal slabs for the unsteady problem and the thickness (in time) of each temporal slab. Slabs are normally taken to be of uniform thickness, although varying thicknesses are permitted. The initial mesh is constructed such that each spatial element in the slab consists of two uniform time-steps to begin with. This is done mainly for the reason of error estimation after the first unsteady solution, where at least a two point stencil is required to construct the BDF2-based time derivative term.

The flow solver computes a solution using this space-time mesh and invokes a local temporal error estimation routine which estimates the temporal discretization error within each element of each slab. Elements within a slab that have temporal discretization error higher than the mean temporal error of the slab as a whole are flagged for refinement.

The mesh adaptation routine takes in the old space-time mesh and the list of space-time elements that have been flagged by the flow solver and constructs a new space-time mesh. Space-time elements that are to be refined are subdivided into two equal elements in the time dimension. A maximum time-step size ratio of two is strictly enforced between neighboring space-time elements in the space dimension in order avoid large jumps in the time-step sizes of neighbors. However, this ratio is currently not enforced in the temporal direction. Once the new space-time mesh has been constructed, it is written to disk and picked up by the flow solver for the next unsteady solution.

Since at any single adaptation cycle, a space-time element is at most subdivided into two, comparisons are made against uniform time-stepping where the number of time-steps is increased by a factor of two and the time-step sizes of all spatial elements are reduced by a factor of two.

IV. Results

A. Case (A): Convection of an isentropic vortex

The first example problem involves the convection of an isentropic vortex through a rectangular domain combined with dynamic mesh deformation. The free-stream conditions for the problem are given by the state $[\rho, u, v, p]$=[1,0.5,0,1]. The initial spatial mesh for the problem consists of 10000 elements and extends from 0 to 14 in the x-direction and from 0 to 7 in the y-direction and is shown in Figure (7). A vortex is seeded in the flow at $[x, y]$=[3.5,3.5] and allowed to convect with the free-stream. Further details on how the vortex is seeded in the flow and the respective parameters for the vortex strength and region of influence can be found in Ref.[23]

The time domain for this problem extends from 0 to 15 in non-dimensional time, indicating that the final position of the vortex is at x=11. For the case of non-uniform time-stepping, the time domain is split into 15 slabs of size 1 each. Since the starting space-time mesh consists of two time-steps of size 0.5 for all spatial elements contained within, the comparison case of uniform time-stepping begins with 30 time-steps of size 0.5 each. At each adaptation cycle, for the uniform time-stepping case, the time-step size for all spatial elements is halved and the number of time-steps is doubled. For the non-uniform case, the local error is used to adapt the time-step sizes within each slab. Both the uniform and non-uniform time-step solutions at the end of the time domain (i.e. t=15) are compared against a uniformly time-stepped reference solution obtained with 32 times the number of time-steps than the finest resolution uniform time-step case, which consists of 960 time-steps. While an exact analytic solution to the vortex convection problem is available, it is not used for comparison purposes since it does not take into account the dissipation of the

vortex due to spatial discretization error. The dynamic motion of the mesh is governed by sinusoidal functions of x, y, t. Although no mesh motion solution is required for this problem, prescribed mesh motion is included in order demonstrate the GCL capabilities of the solver. The perturbation of every single node in the space-time mesh is uniquely defined by analytic mesh motion functions, details of which can be found in Ref.[24] Figure (8) shows the density contours of the solution to the unsteady problem at the final time of t=15 and also illustrates the deformation of the mesh compared to the baseline or starting configuration. This particular solution is that after six adaptation cycles of the non-uniform time-stepping solver. Both uniform and non-uniform time-stepping cases were terminated after 6 adaptation cycles.

Figure (9(a)) compares the error in the solution of the uniform time-stepping case and the non-uniform time-stepping case at each adaptation cycle and indicates good agreement. Figures (9(b)) and (9(c)) compare the solution errors for the uniform and non-uniform time-stepping cases to CPU cost and to the total number of degrees-of-freedom required to solve the problem. The number of degrees-of-freedom in the case of uniform time-stepping is the product of the number of spatial elements and the number of time-steps, while for the non-uniform time-stepping case, it is the sum of space-time elements over all temporal slabs. For this particular problem, it can be seen from the plots that the spatially non-uniform time-stepping procedure is able to achieve similar error levels as uniform time-stepping with approximately 25% less computational expense and approximately one fourth of the number degrees-of-freedom. Figure (10) compares the density along the centerline of the spatial mesh at various time-levels between the uniform and non-uniform time-stepping cases and indicates excellent agreement. Figures (11(a)) and (11(b)) indicate the distribution of the local error at the top of the first temporal slab and the top of the last (15th) temporal slab after the final (6th) adaptation cycle. The distributions shown in these figures include the local error of all the space-time elements laying underneath the spatial elements shown in the plots but within the same slab. Figures (11(c)) and (11(d)) compare the number time-steps a spatial element takes within the slab in slabs 1 and 15 after the final adaptation cycle. It can be clearly seen that most of the spatial elements take no more than 5 time-steps while spatial elements where the vortex has a strong influence take nearly 60 time-steps.

B. Case (B): Transonic pitching airfoil

The second example is that of a transonic pitching NACA64A010 airfoil. The airfoil pitches around its quarter-chord location in a free-stream Mach number of 0.8 with a mean angle-of-attack of zero. The amplitude of pitch is 2.5 degrees and the reduced frequency is 0.1. The time domain for this problem was chosen such that one pitch period is completed starting from a zero angle-of-attack. The non-uniform time-stepping case consists of 16 equally sized temporal slabs of temporal thickness 1.96349540 in non-dimensional time. Since the starting space-time mesh within each slab consists of each spatial element taking two time-steps, the uniform time-stepping case begins with 32 time-steps, each of time-step size 0.9817478. The initial condition for this problem is set from an approximate periodically steady-state solution at zero angle-of-attack. Figure (12) shows the spatial mesh for this problem and consists of approximately 6600 spatial elements. The mesh motion equations are solved for this problem with prescribed displacements applied to the surface of the airfoil. Since different mesh motion equations are solved for the non-uniform and uniform time-stepping cases, there is no guarantee that the interior mesh points match up between these cases at the end of the time domain. However, the boundaries have prescribed displacements and they match between the cases. For this reason, an estimate of the error in the solution cannot be made in the same manner as the previous example problem. As an alternative, the solution error in this problem is estimated by taking the integrated L_2 norm difference between the computed pressure coefficient distributions for the uniform and non-uniform cases against a reference pressure coefficient distribution. The reference pressure coefficient distribution is obtained using uniform time-stepping with approximately 16000 time-steps. Adaptation was terminated after 6 cycles for both the uniform and non-uniform time-stepping cases. Figure (13) compares the pressure coefficient distributions between the uniform and non-uniform cases at the end of the time domain of the final adaptation cycle and qualitatively shows excellent agreement.

Figure (14(a)) compares the error in the solution measured as described above, between the spatially non-uniform and uniform time-stepping cases at each adaptation cycle. For this particular problem, non-uniform time-stepping performs quite poorly compared to the uniform time-stepping method. Similar trends are observed in Figures (14(b)) and (14(c)), which compare solution error to the computational cost and total degrees-of-freedom.

There are two primary reasons which could possibly explain this behavior, one being the definition of the local error indicator and the other being the mesh motion solution. It was assumed that small geometric variations would have a negligible impact on the estimate of the local error. Unlike the earlier vortex convection example, where all spatial elements are nearly the same size, the pitching airfoil problem has large variations in spatial element sizes. Spatial elements close to the airfoil are significantly smaller than the spatial elements in the far field. This difference in element size has a tendency to pollute the error estimate leading to incorrect adaptation. It can be seen from the

error plots that although degrees-of-freedom have significantly increased in each of the adaptation cycles, the error in the solution does not decrease as fast as uniform adaptation, leading to the theory that adaptation is occurring in the wrong locations due to inaccurate error estimates. The adaptation shown in Figure (15) further strengthens this theory. The figure shows the number of time-steps the spatial elements take in slab 8 at the final adaptation cycle for this problem. There are multiple regions significantly far away from the airfoil that take nearly as many time-steps as elements close to the airfoil indicating shortcomings of the error indicator.

The other aspect is the mesh motion solution for the non-uniform time-stepping case. While the size of the mesh motion system remains the same at each time-step for the uniform time-stepping case, the size of the mesh motion system constantly increases for each slab as adaptation progresses in the non-uniform time-stepping case. Since only Gauss-Seidel iterations are used to solve the linear system, the convergence rate for the mesh solution significantly slows down as the system size increases. This directly reflects on the overall cost required for the non-uniform time-stepping case.

In spite of these shortcomings, Figures (16(a)) to (16(b)) indicate general trends near the airfoil which are in accordance with expectations. The local error distributions show clearly, a high level of error tracking the moving shock waves on the upper and lower surfaces of the airfoil, while the corresponding adaptations of the time-steps indicate spatial elements in the those areas taking significantly more time-steps.

V. Concluding Remarks and Future Work

A space-time finite-volume formulation was developed to treat both space and time dimensions in a unified manner. The method permits non-uniform advancement of spatial elements in time and offers the possibility reducing overall computational expense in unsteady flow solutions. The first example problem of a convecting vortex clearly shows that reduction in cost with almost no loss in solution accuracy is possible by varying the time-step size spatially. In regards to the second example problem, several issues remain to be addressed. The problem of increasing mesh motion solution cost can easily be addressed by implementing multigrid to remove system size dependence on convergence. Both adaptation examples presented in the paper utilized a crude form of local error estimation to determine space-time regions that require higher temporal resolution. While this worked reasonably well in the first example problem, there are serious shortcomings to using such a method when measuring solution accuracy with respect to surface integrated quantities such as that in the second example. Extension of the method to higher-order time-integration schemes is essential in order to improve solution accuracy and to construct a better local error indicator. In addition to better local error indicators, the results from the second example also emphasize the need for goal-based error indicators.

Prior work on adapting the time-step size at different time levels but uniformly for all spatial elements on the basis of functional relevant temporal discretization error computed via the adjoint equation, has shown such adaptation to be more economical than uniform time-step sizes in space and time.[15,16] It is expected that applying the adjoint weighted residual method to determine functional relevant error in a space-time formulation and adapting the time-step size locally for each spatial element on the basis of such an error distribution will likely yield significant improvements in the results both in terms of accuracy and cost.

Another research topic that needs to be addressed is the development of a multigrid algorithm that is applicable to space-time meshes. While a multigrid solution option was available in the spatially uniform time-stepping case, it was disabled for comparison with spatially non-uniform time-stepping results where currently no multigrid option exists.

Ultimately, the developed method for solving unsteady problems should find applications particularly in the context of rotorcraft and wind turbines, where large differences exist between the flow close to the hub and flow close to the tips of the blades.

VI. Acknowledgements

This work was sponsored by the Office of Naval Research under grant N00014-09-1-1060 and by the National Science Foundation under grant OCI-0960490.

References

[1]Jameson, A., Schmidt, W., and Turkel, E., "Numerical Solutions of the Euler Equations by Finite Volume Methods Using Runge-Kutta Time-Stepping Schemes," *AIAA 14th Fluid and Plasma Dynamic Conference, Palo Alto, CA*, 1981, AIAA Paper 81–1259.

[2]Jameson, A., "Time Dependent Calculations Using Multigrid, with Applications to Unsteady Flows Past Airfoils and Wings," *AIAA 10th Computational Fluid Dynamics Conference, Honolulu, HI*, 1991, AIAA Paper 91–1596.

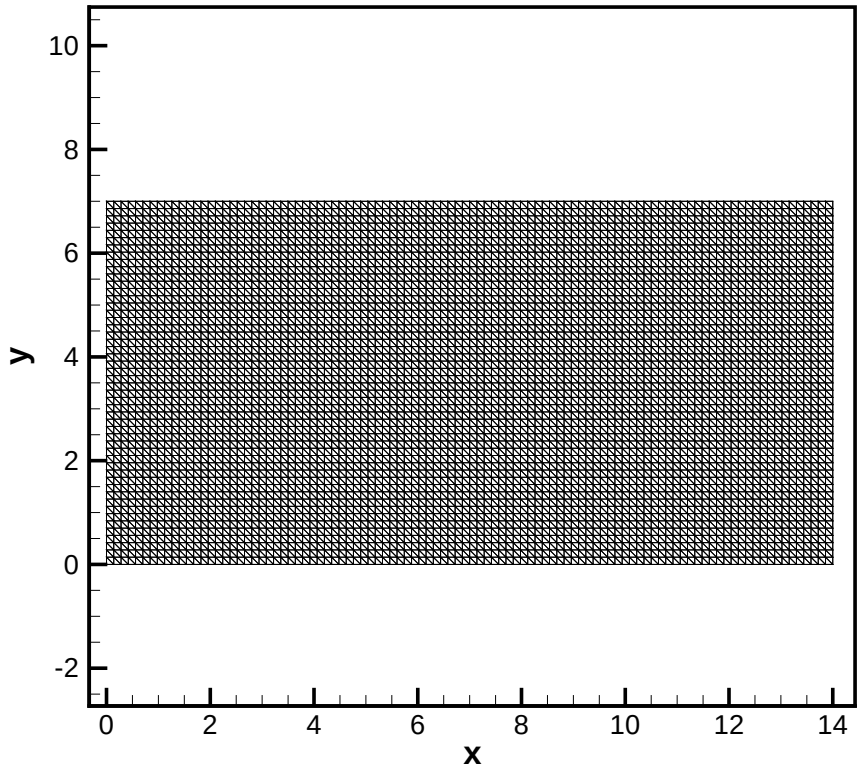

Figure 7. Initial spatial computational mesh consisting of 10000 spatial elements for the vortex convection example problem.

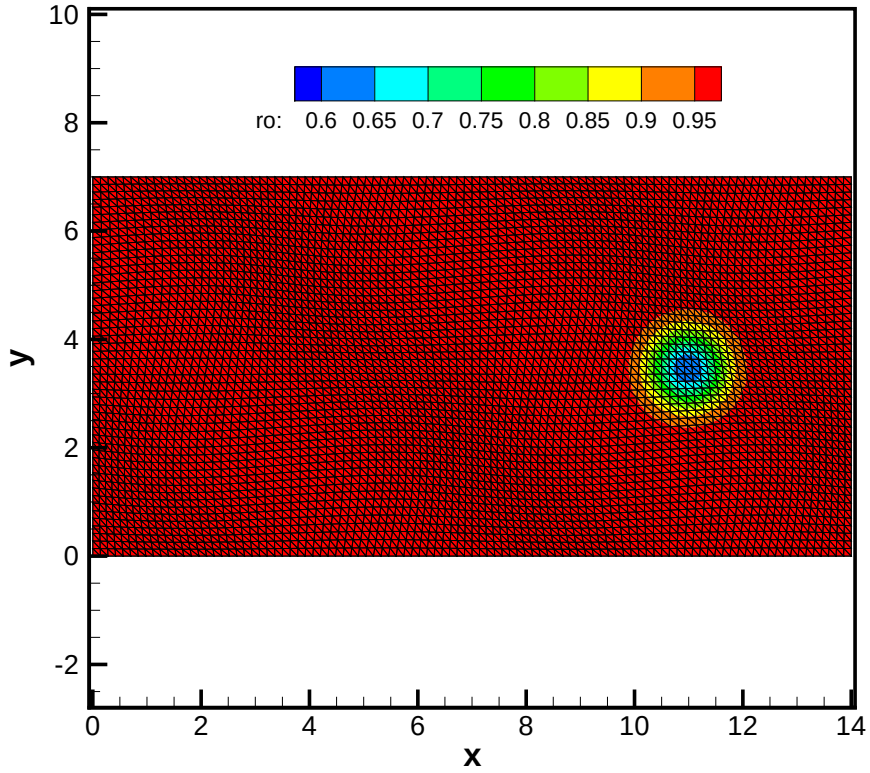

Figure 8. Density contours for the vortex convection problem at the final time of t=15. This solution is from the spatially non-uniform time-stepping case after 6 adaptation cycles.

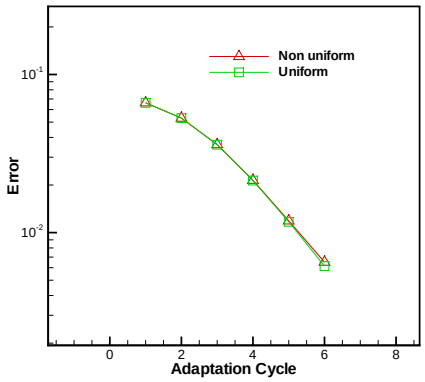

(a) Solution error comparison at each adaptation cycle.

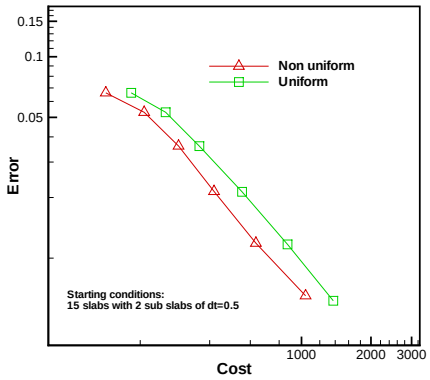

(b) Solution error convergence with respect to CPU cost.

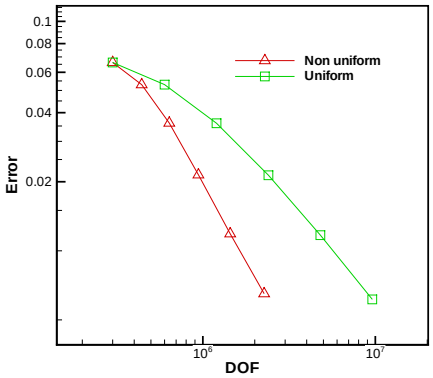

(c) Solution error convergence with respect to total degrees-of-freedom.

Figure 9. Comparison of solution error between spatially uniform and non-uniform time-stepping for the convecting vortex example problem.

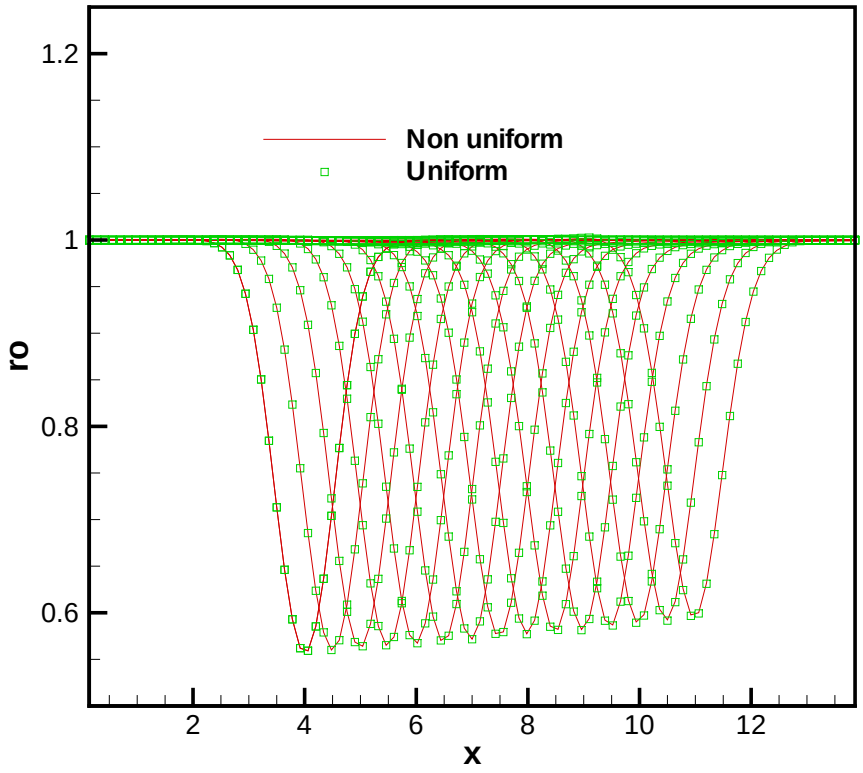

Figure 10. Comparison of mesh centerline density at different time-levels for the convecting vortex example problem.

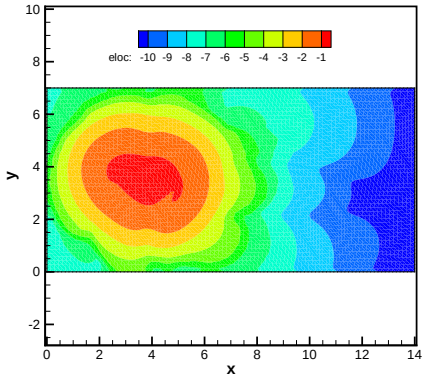

(a) Distribution of local error at the top of slab 1.

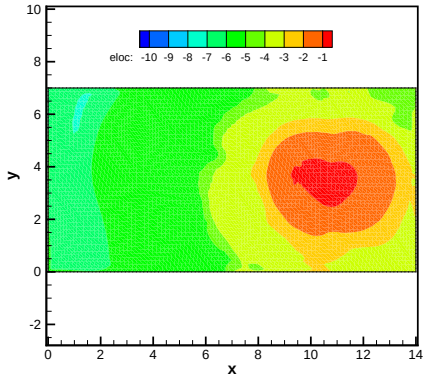

(b) Distribution of local error at the top of slab 15.

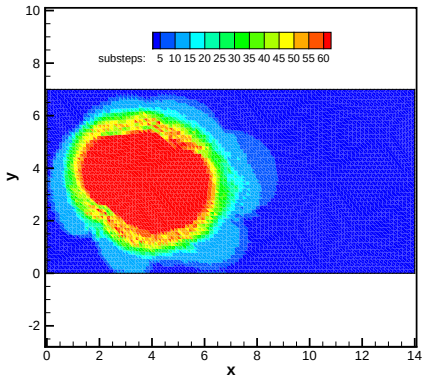

(c) Number of time-steps per spatial element at the top of slab 1.

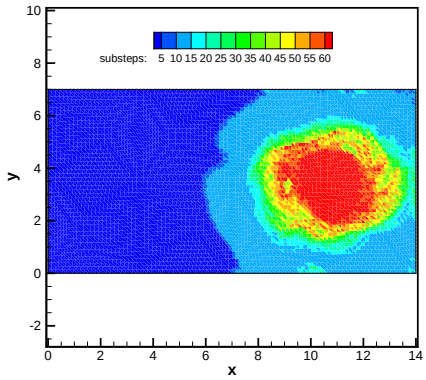

(d) Number of time-steps per spatial element at the top of slab 15.

Figure 11. Comparison of local error distribution and number of time-steps per spatial element at the top of slabs 1 and 15 for the convecting vortex example problem. The plots are at the final adaptation cycle.

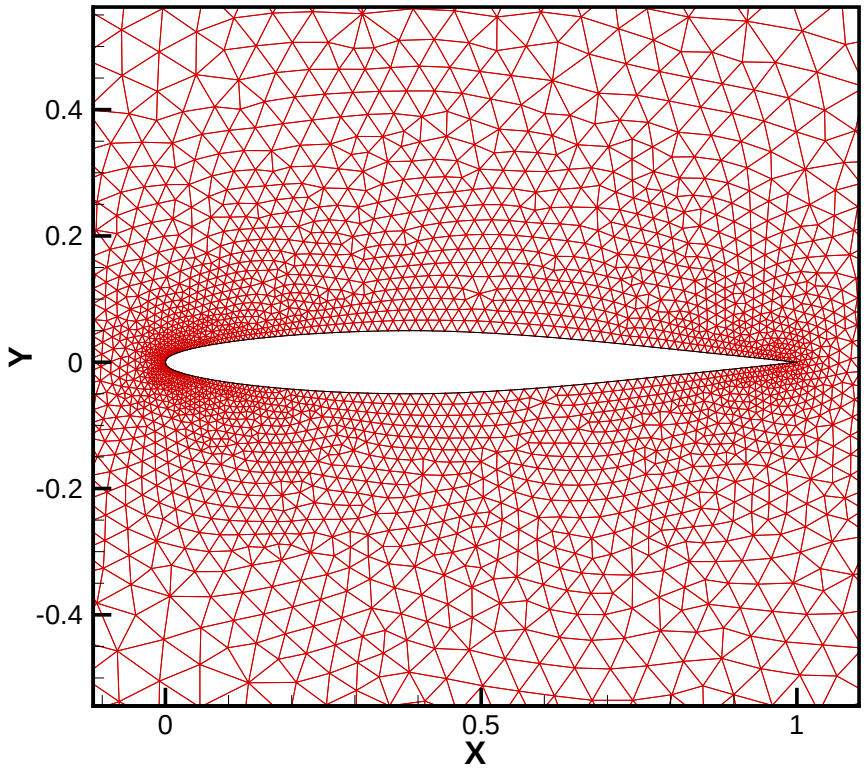

Figure 12. Computational mesh consisting of 6601 elements for the transonic pitching airfoil example.

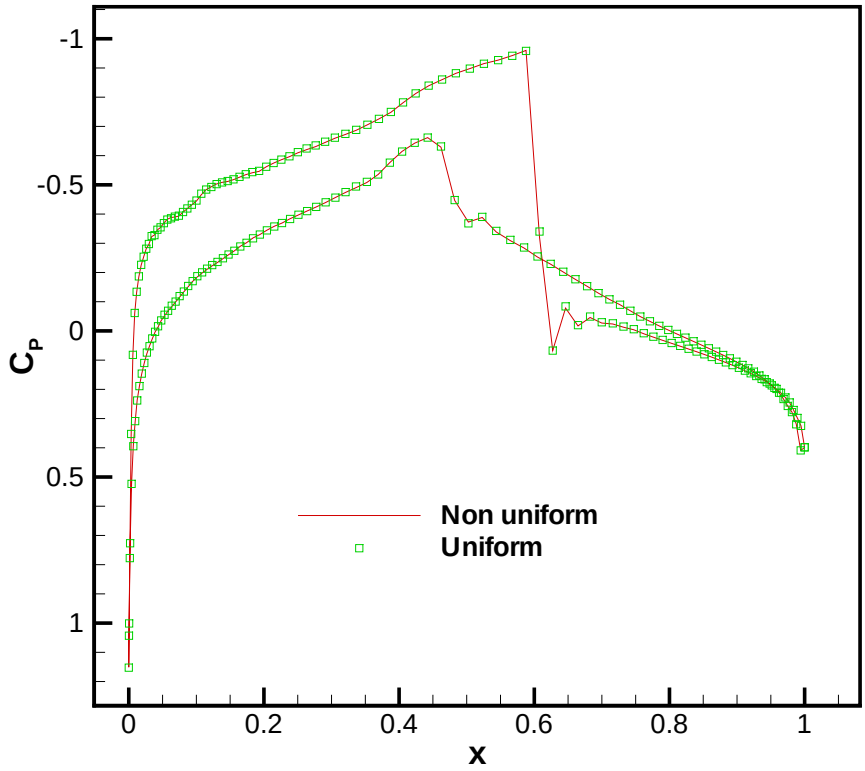

Figure 13. Comparison of the surface pressure coefficient distribution between the spatially uniform and non-uniform time-stepping case at the final adaptation cycle for transonic pitching airfoil example.

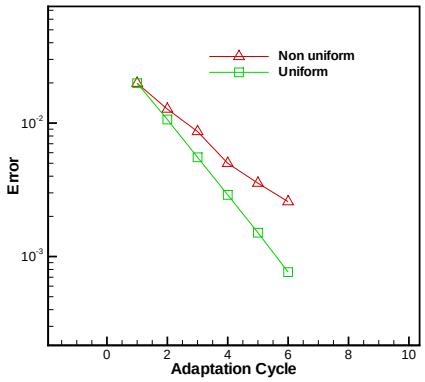

(a) Solution error comparison at each adaptation cycle.

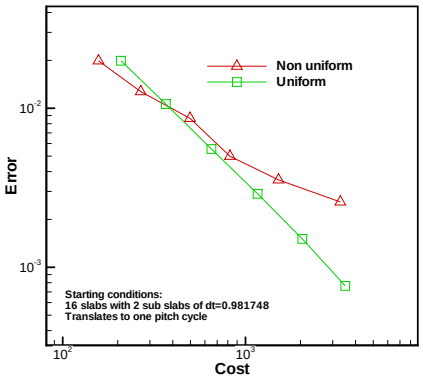

(b) Solution error comparison with respect to CPU cost.

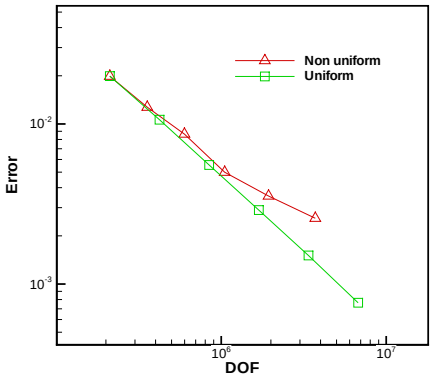

(c) Solution error comparison with respect to total degrees-of-freedom.

Figure 14. Comparison of solution error between spatially uniform and non-uniform time-stepping for the transonic pitching airfoil problem.

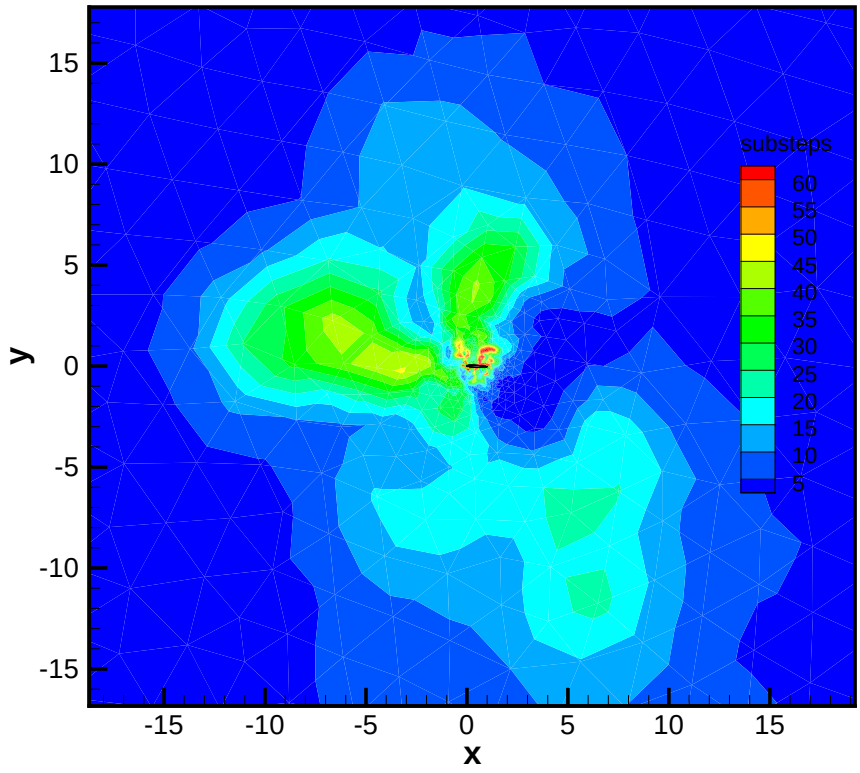

Figure 15. Local error distribution for the transonic pitching airfoil example on top slab 8 at the 5th adaptation cycle.

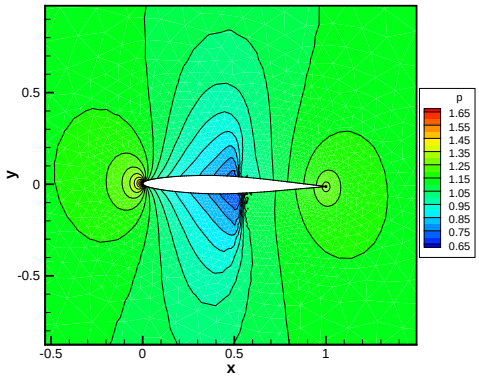

(a) Pressure contours on top of slab 1.

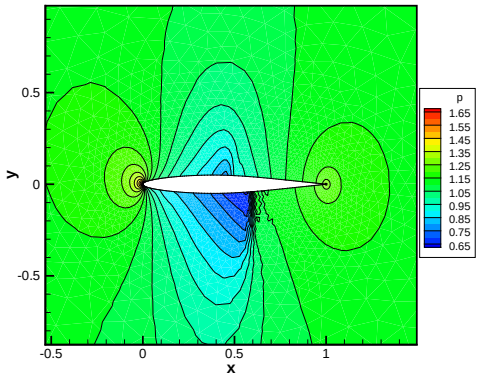

(b) Pressure contours on top of slab 16.

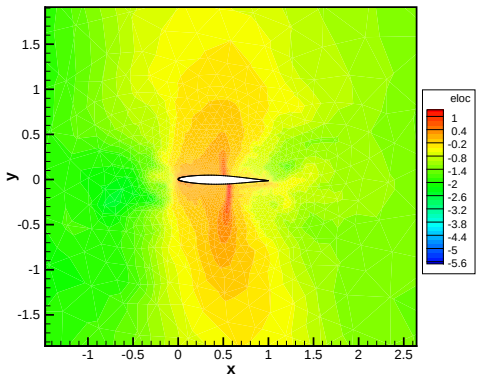

(c) Local error distribution on top of slab 1.

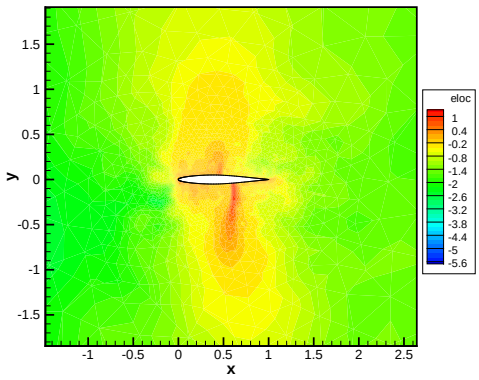

(d) Local error distribution on top of slab 16.

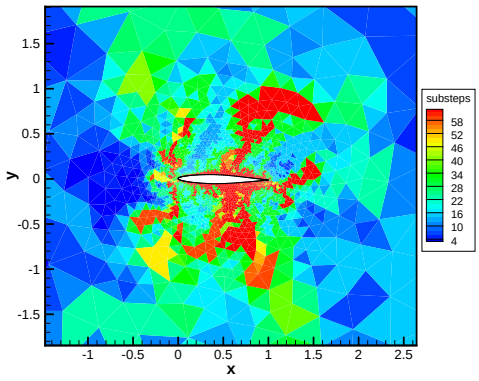

(e) Number of time-steps per spatial element on top of slab 1.

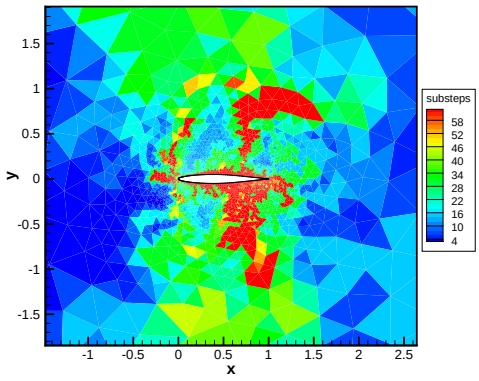

(f) Number of time-steps per spatial element on top of slab 15.

Figure 16. Comparison of local error distribution and number of time-steps per spatial element at the top of slabs 1 and 16 for the transonic pitching airfoil example. The plots are at the final adaptation cycle.

[3]Carpenter, M. H., Viken, S., and Nielsen, E., "The Efficiency of High-Order Temporal Schemes," AIAA Paper 2003-0086.

[4]Carpenter, M. H. and Vatsa, V., "Higher Order Temporal Schemes with Error Controllers for Unsteady Navier-Stokes Equations," *17th AIAA Computational Fluid Dynamics Conference, Toronta, Ontario, Canada, June 2005*, 2005, AIAA Paper 2005–5245.

[5]Bijl, H., Carpenter, M., Vatsa, V., and Kennedy, C., "Implicit Time Integration Schemes for the Unsteady Compressible Navier-Stokes Equations - Laminar Flow," *Journal of Computational Physics*, Vol. 179-1, 2002, pp. 313–329.

[6]Mavriplis, D. and Yang, Z., "Construction of the discrete geometric conservation law for high-order time-accurate simulations on dynamic meshes," *Journal of Computational Physics*, Vol. 213, 2006, pp. 557–573.

[7]Yang, Z. and Mavriplis, D. J., "Higher-Order Time Integration Schemes for Aeroelastic Applications on Unstructured Meshes," *AIAA Journal*, Vol. 45-1, January 2007, pp. 138–150.

[8]Nadarajah, S., McMullen, M., and Jameson, A., "Non-Linear Frequency Domain Based Optimum Shape Design for Unsteady Three-Dimensional Flow," *Proceedings of the 44th Aerospace Sciences Meeting and Exhibit, Reno NV*, 2006, AIAA Paper 2006–387.

[9]Nadarajah, S., McMullen, M., and Jameson, A., "Optimal Control of Unsteady Flows Using Time Accuraate and Non-Linear Frequency Domain Methods," *33rd AIAA Fluid Dynamics Conference and Exhibit, Orlando, FL, June 23-26,*, 2003, AIAA Paper 2003–3875.

[10]Jameson, A., "Acceleration of Transonic Potential Flow Calculations on Arbitrary Meshes by the Multiple Grid Method," *Fourth AIAA Computational Fluid Dynamics Conference, Williamsburg, VA*, 1979, AIAA Paper 79–1458.

[11]Mavriplis, D., "Multigrid Techniques for Unstructured Meshes," *Notes prepared for 26th Computational Fluid Dynamics Lecture Series Program of the von Karman Institute of Fluid Dynamics, Rhode St Genese, Belgium*, 1995.

[12]Melson, N. D., Sanetrik, M. D., and Atkins, H. L., "Time-accurate Navier-Stokes calculations with multigrid acceleration," *6th Copper Mountain Conf. on Multigrid Methods*, 1993, pp. 423–439, NASA Conference Publication 3224.

[13]Butcher, J. C., *Numerical methods for ordinary differential equations*, Wiley, Chicester, UK, 2003.

[14]Lambert, J. D., *Numerical methods for ordinary differential systems*, Wiley, Chicester, UK, 1991.

[15]Mani, K. and Mavriplis, D. J., "Discrete Adjoint based Time-Step Adaptation and Error Reduction Unsteady Flow Problems," *18th AIAA Computational Fluid Dynamics Conference , Miami FL*, 2007, AIAA Paper 2007–3944.

[16]Mani, K. and Mavriplis, D. J., "Error Estimation and Adaptation for Functional Outputs in Time-Dependent Flow Problems," *47th AIAA Aerospace Sciences Meeting including The New Horizons Forum and Aerospace Exposition, Orlando, Florida, Jan. 5-8, 2009*, 2009, AIAA Paper 2009–1495.

[17]van der Vegt, J. J. W. and van der Ven, H., "Space–time discontinuous Galerkin finite element method with dynamic grid motion for inviscid compressible flows: I. general formulation," *Journal of Computational Physics*, Vol. 182-2, 2002, pp. 546–585.

[18]Abedi, R., Chung, S.-H., Erickson, J., Fan, Y., Garland, M., Guoy, D., Haber, R., Sullivan, J. M., Thite, S., and Zhou, Y., "Spacetime meshing with adaptive refinement and coarsening," *Annual Symposium on Computational Geometry, Proceedings of the twentieth annual symposium on Computational geometry Brooklyn, New York, USA*, 2004.

[19]Barth, T. J., "Space-Time Error Representation and Estimation in Navier-Stokes Calculations," *Lecture Notes in Computational Science and Engineering*, Vol. 56, 2007.

[20]Mavriplis, D. J., "Unstructured-Mesh Discretizations and Solvers for Computational Aerodynamics," *AIAA Journal*, Vol. 46-6, June 2008, pp. 1281–1298.

[21]Batina, J. T., "Unsteady Euler Airfoil Solutions Using Unstructured Dynamic Meshes," *AIAA Journal*, Vol. 28-8, August 1990, pp. 1381–1388.

[22]Mavriplis, D. J., "Multigrid Solution of the Discrete Adjoint for Optimization Problems on Unstructured Meshes," *AIAA Journal*, Vol. 44-1, January 2006, pp. 42–50.

[23]Wang, L. and Mavriplis, D. J., "Implicit solution of the unsteady Euler equations for high-order accurate discontinuous Galerkin discretizations," *Journal of Computational Physics*, Vol. 225-2, 2007, pp. 1994–2015.

[24]Nastase, C. R. and Mavriplis, D. J., "On the Geometric Conservation Law for High-Order Discontinuous Galerkin Discretizations on Dynamically Deforming Meshes," *46th Aerospace Sciences Meeting and Exhibit, Reno NV*, 2008, AIAA Paper 2008–778.